Supplementary Information:

Efficient and Stable Formamidinium-Caesium Perovskite Solar Cells and Modules from Lead Acetate-Based Precursor

Jie Zhao,[1,2] Sebastian O. Fürer,[1,2] David P. McMeekin,[1,2] Qingdong Lin,[1,2] Pin Lv,[3] Jisheng Ma,[4,5] Wen Liang Tan,[4] Chao Wang,[4] Anthony S. R. Chesman,[6,7] Boer Tan,[1,2] Huiyu Yin,[8] Andrew D. Scully,[6] Christopher R. McNeill,[4] Wenxin Mao,[1,2] Jianfeng Lu,[3,8]* Yi-Bing Cheng,[8,9] Udo Bach[1,2,10]**

[1] Department of Chemical and Biological Engineering, Monash University, Victoria 3800, Australia

[2] ARC Center of Excellence in Exciton Science, Monash University, Victoria 3800, Australia

[3] State Key Laboratory of Silicate Materials for Architectures, Wuhan University of Technology, Wuhan 430070, China

[4] Department of Materials Science and Engineering, Monash University, Victoria 3800, Australia

[5] Monash X-ray Platform, Monash University, Victoria 3800, Australia

[6] CSIRO Manufacturing, Clayton, Victoria 3168, Australia

[7] The Melbourne Centre for Nanofabrication, Victorian Node of the Australian National Fabrication Facility, Clayton, Victoria 3168, Australia

[8] Foshan Xianhu Laboratory of the Advanced Energy Science and Technology Guangdong Laboratory, Foshan 528216, PR China

[9] State Key Laboratory of Advanced Technology for Materials Synthesis and Processing, Wuhan University of Technology, Wuhan 430070, China

[10] Lead Contact

**Correspondence: Wenxin.Mao@monash.edu*

**Correspondence: Jianfeng.lu@whut.edu.cn*

***Correspondence: Udo.Bach@monash.edu*

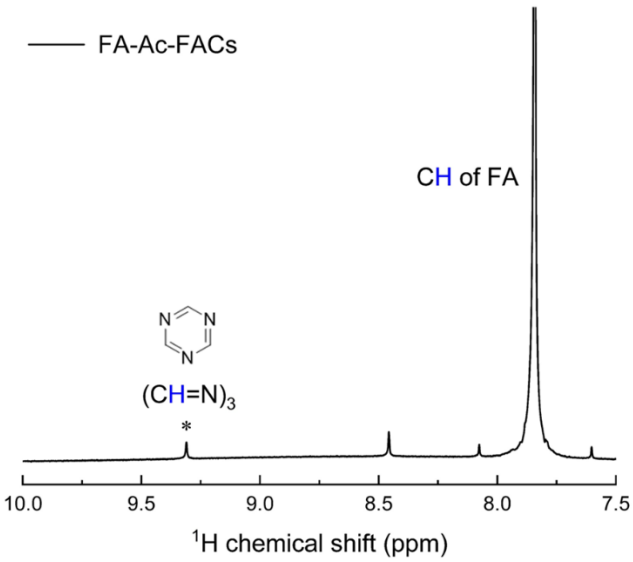

Fig. S1. Solution ^{1}H-NMR spectrum of the $FA_{0.83}Cs_{0.17}Pb(I_{0.9}Br_{0.1})_3$ films made from FA-Ac-FACs. The films were dissolved in DMSO-d_6 for the measurement. In addition to the peaks from FA at 7.85 ppm, we found an additional peak at 9.31 ppm that can be assigned to *sym*-triazine.

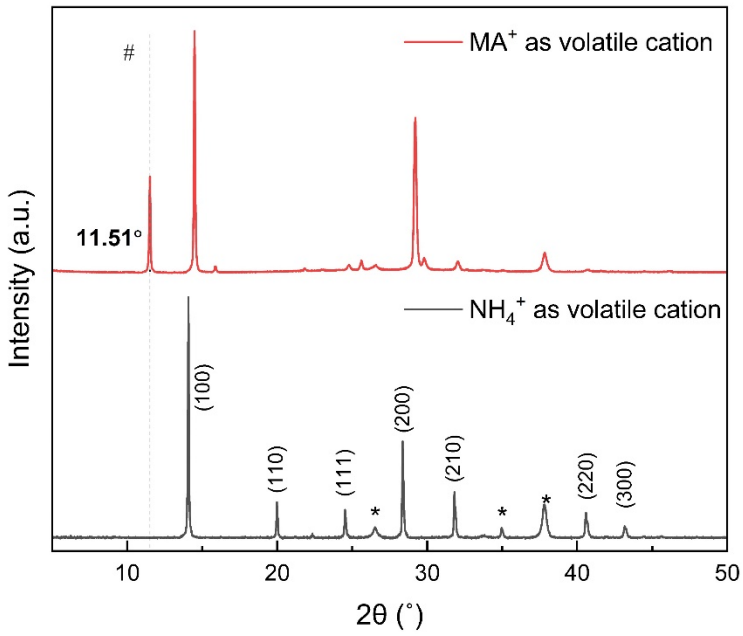

Fig. S2. XRD patterns of the FACs perovskite films made from MA-Ac-FACs (red) and A-Ac-FACs (black). Peaks marked with * and # are assigned to FTO and *N*-methyl formamidinium iodide (MFAI), respectively.

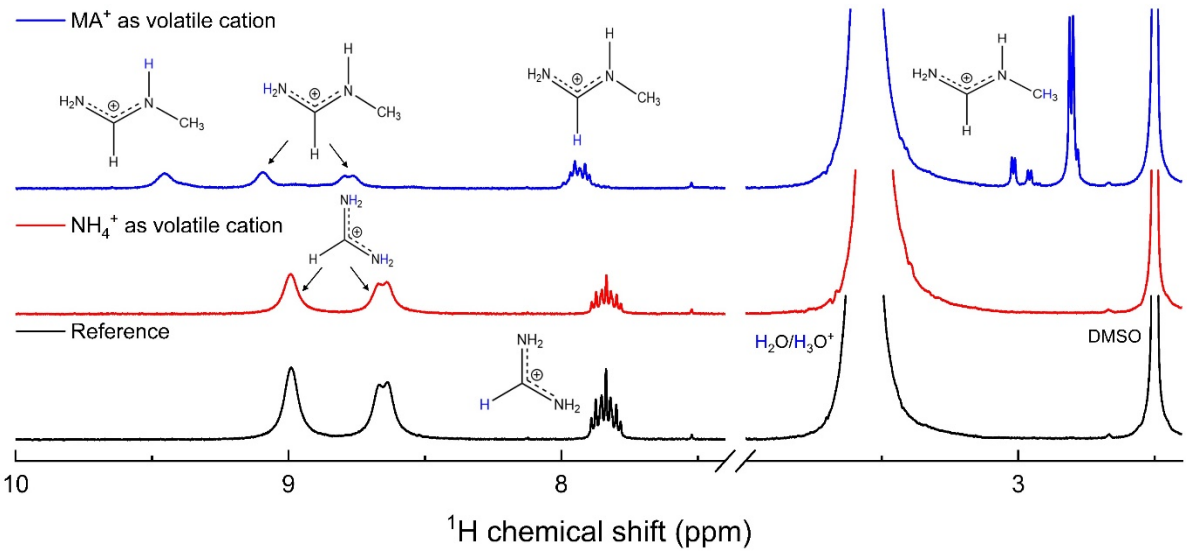

Fig. S3 Solution ^{1}H NMR results of dissolved $FA_{0.83}Cs_{0.17}Pb(I_{0.9}Br_{0.1})_3$ films made from MA-Ac-FACs (blue) and A-Ac-FACs (red) and reference $FA_{0.83}Cs_{0.17}Pb(I_{0.9}Br_{0.1})_3$ film made via the PbI_2 route (black). The films were directly dissolved in DMSO-d_6 and spiked with HI for the measurement.

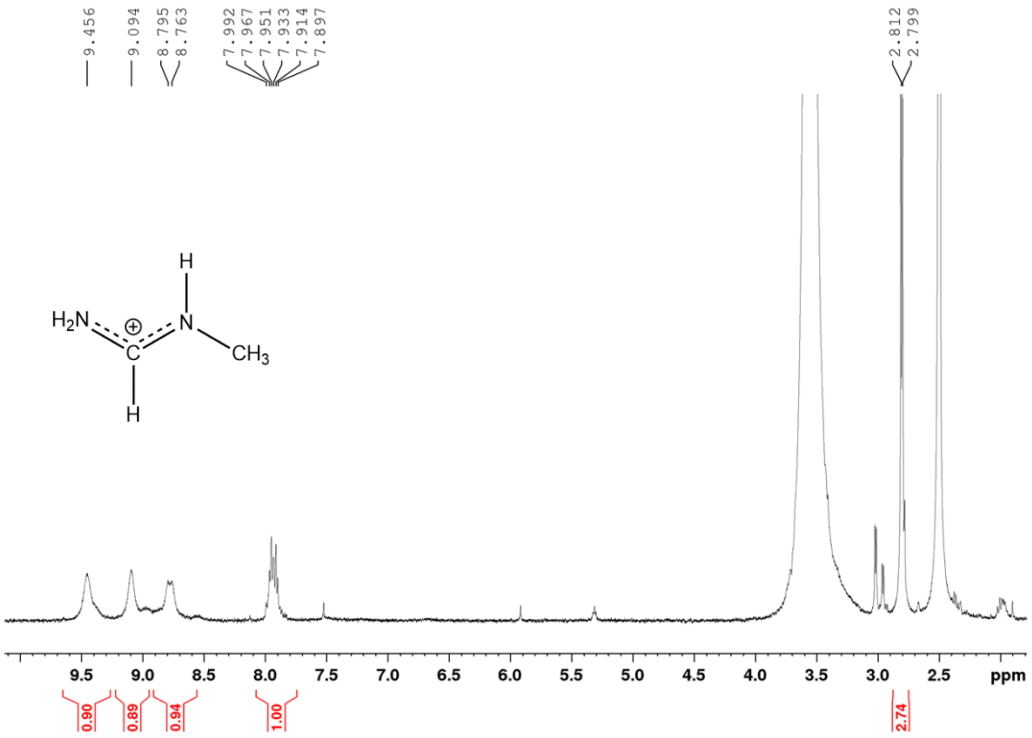

Fig. S4. Solution ^{1}H-NMR spectrum of the $FA_{0.83}Cs_{0.17}Pb(I_{0.9}Br_{0.1})_3$ films made from $PbAc_2$ route when using MA^+ as volatile cation. The films were dissolved in DMSO-d_6 and spiked with HI for the measurement.

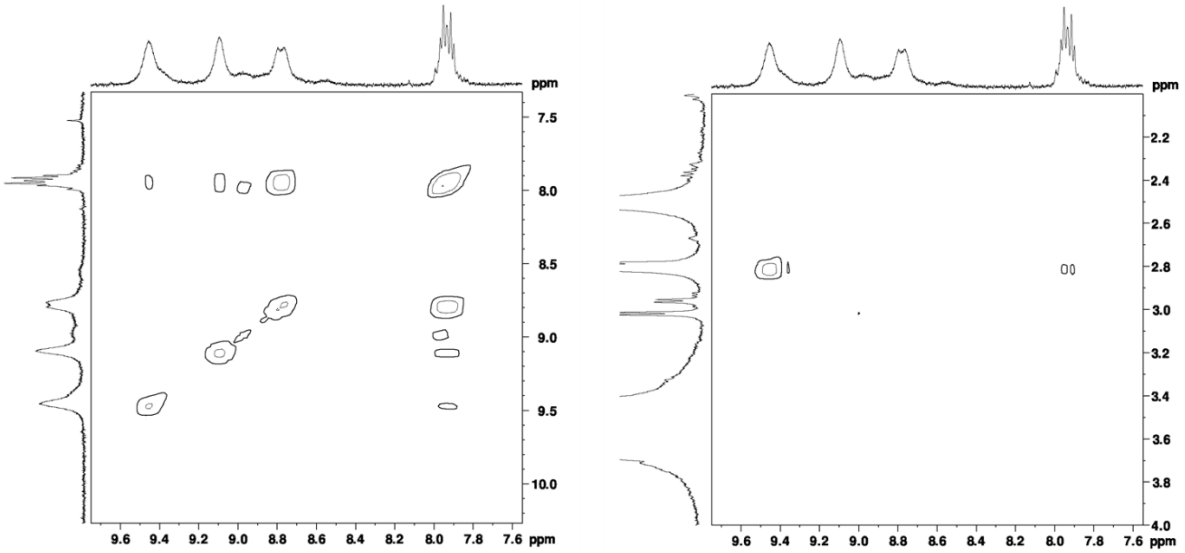

Fig. S5. ^{1}H-^{1}H COSY NMR spectrum of $FA_{0.83}Cs_{0.17}Pb(I_{0.9}Br_{0.1})_3$ films made from $PbAc_2$ route using MA^+ as volatile cation. The films were dissolved in DMSO-d_6 for the measurement. The left part shows the correlation of the $H^{\underline{CH}}$ with $H^{\underline{NH}}$ protons while the right part shows coupling between $H^{\underline{CH}}$ and H^{Me}. The films were directly dissolved in DMSO-d_6 and spiked with HI for the measurement.

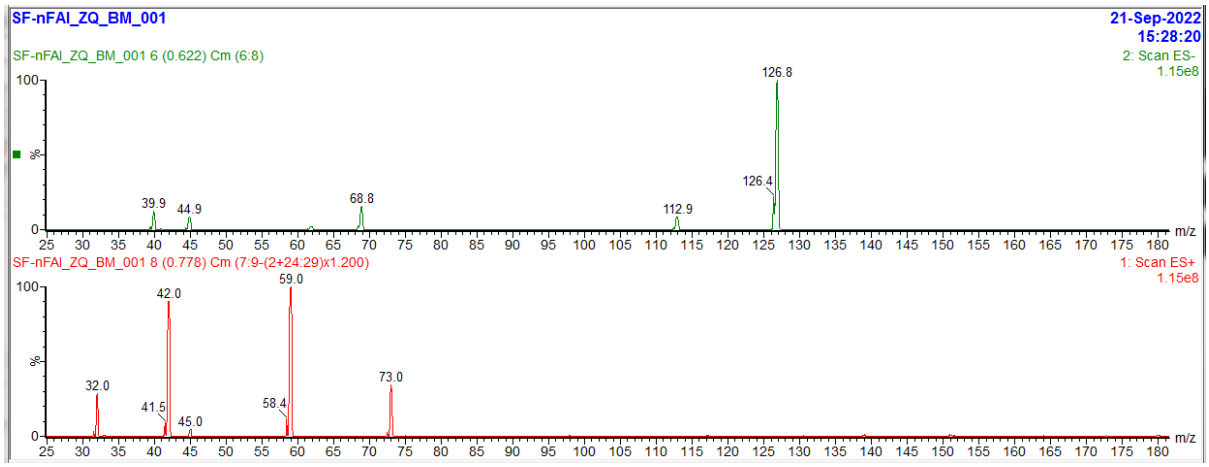

Fig. S6. Mass spectrum results of $FAPbI_3$ films made from $PbAc_2$ route using MA^+ as volatile cation. The films were dissolved in methanol for the measurement. The top section contains the anions, the m/z peak at 126.8 belongs to iodide. The bottom section contains cations. (m/z 32.0: MA, m/z 45.0: FA, m/z 59.0: MFA, m/z 73: DMFA).

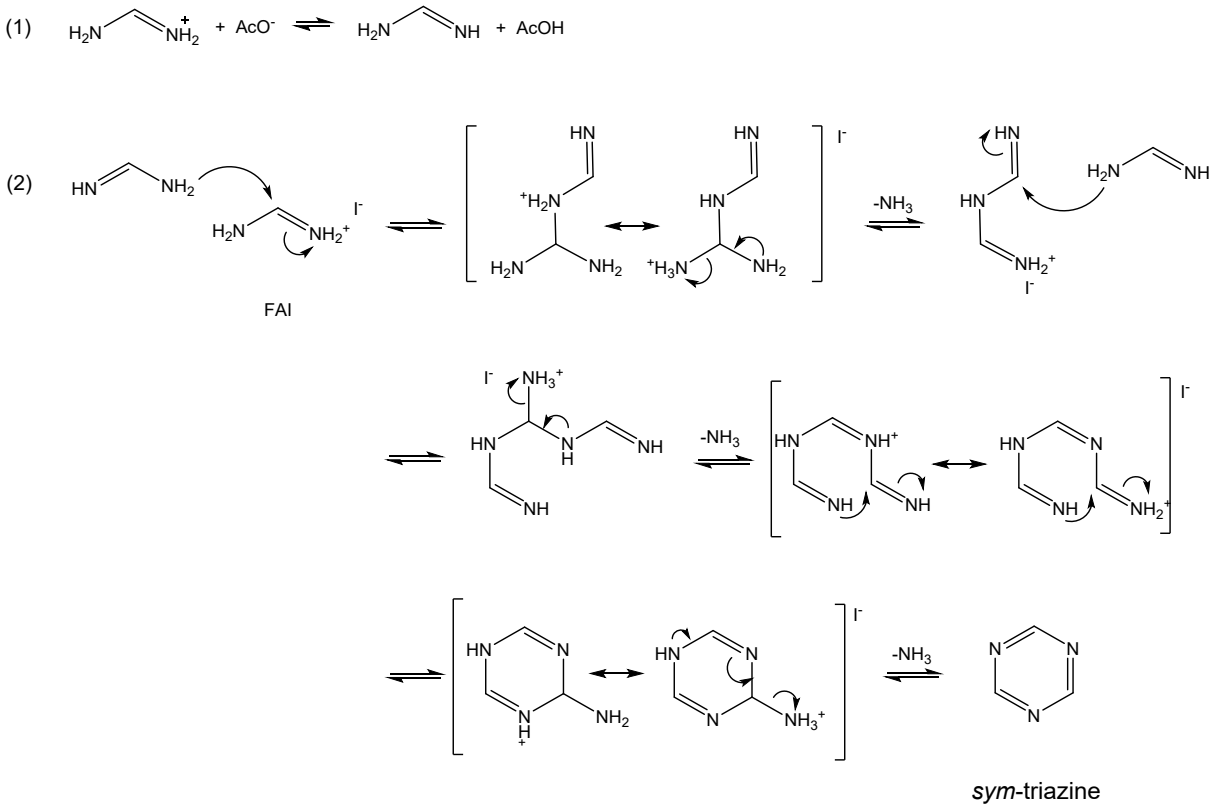

Fig. S7. Proposed side reaction pathway in the precursor solution of FA-Ac-FACs based on Wang et al. and Grundamm and Kreutzberger. (1, 2)

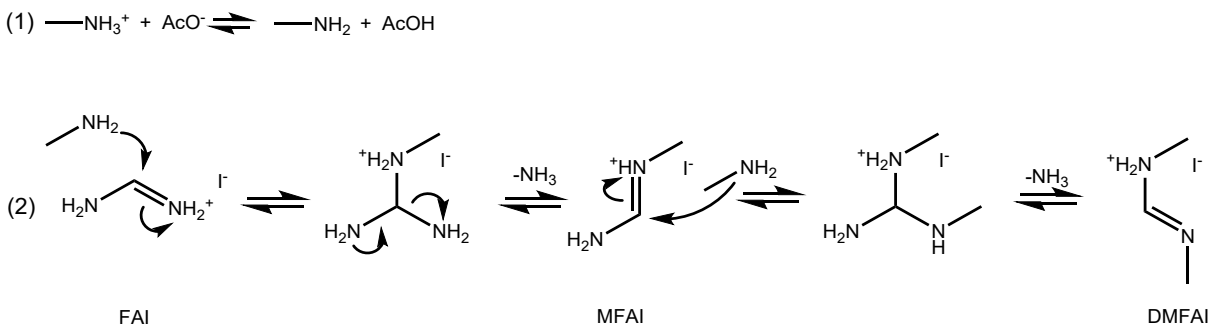

Fig. S8. Proposed side reaction pathway in the precursor solution of MA-Ac-FACs based on Wang et al. (1)

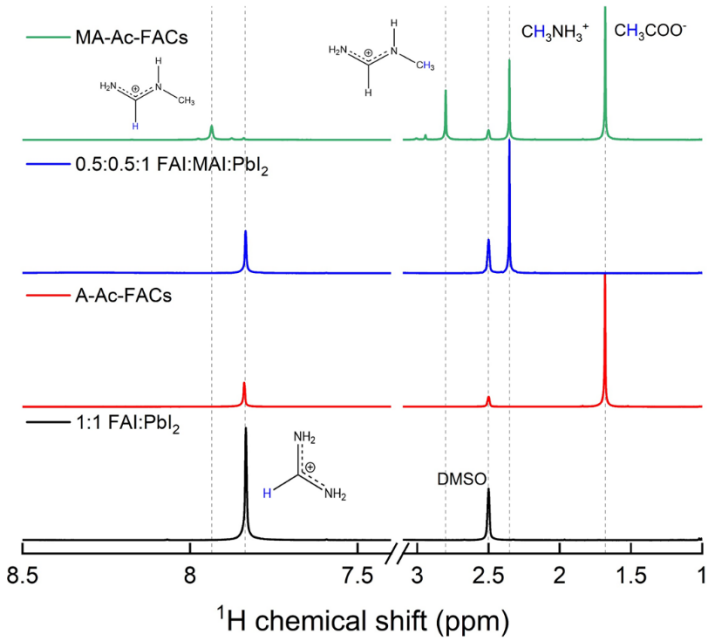

Fig. S9. Solution ^{1}H NMR results of the perovskite precursor solution. Green: MA-Ac-FACs, Blue: FAMA perovskite PbI_2 route, Red: A-Ac-FACs, Black: FA perovskite PbI_2 route. The solutions were directly prepared in DMSO-d_6 for the measurement.

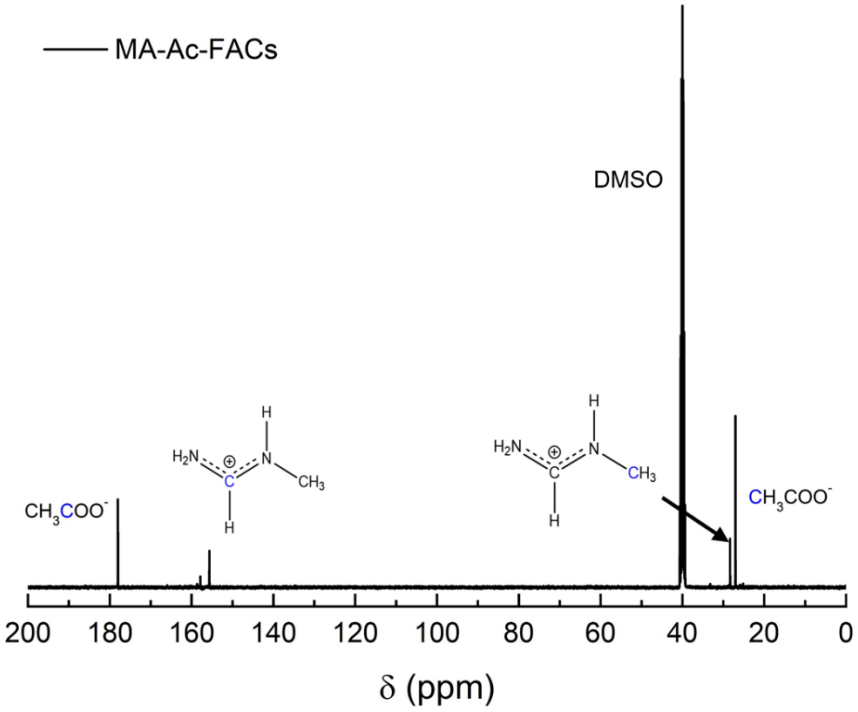

Fig. S10. Solution ^{13}C-NMR spectrum of MA-Ac-FACs precursor solution. The solutions were prepared in DMSO-d_6 for the measurement.

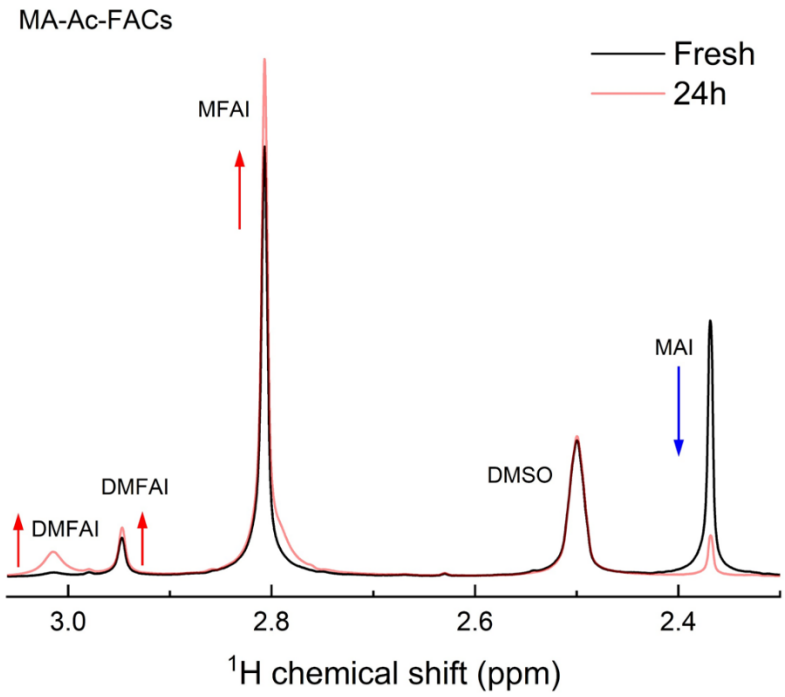

Fig. S11. Superimposed ^{1}H-NMR spectra of MA-Ac-FACs precursor solution as a function of aging time. The solutions were prepared in DMSO-d_6 for the measurements.

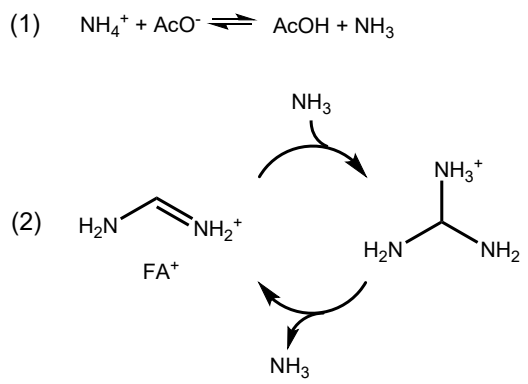

Fig. S12. Proposed reaction pathway in the precursor solution of (A-Ac-FACs).

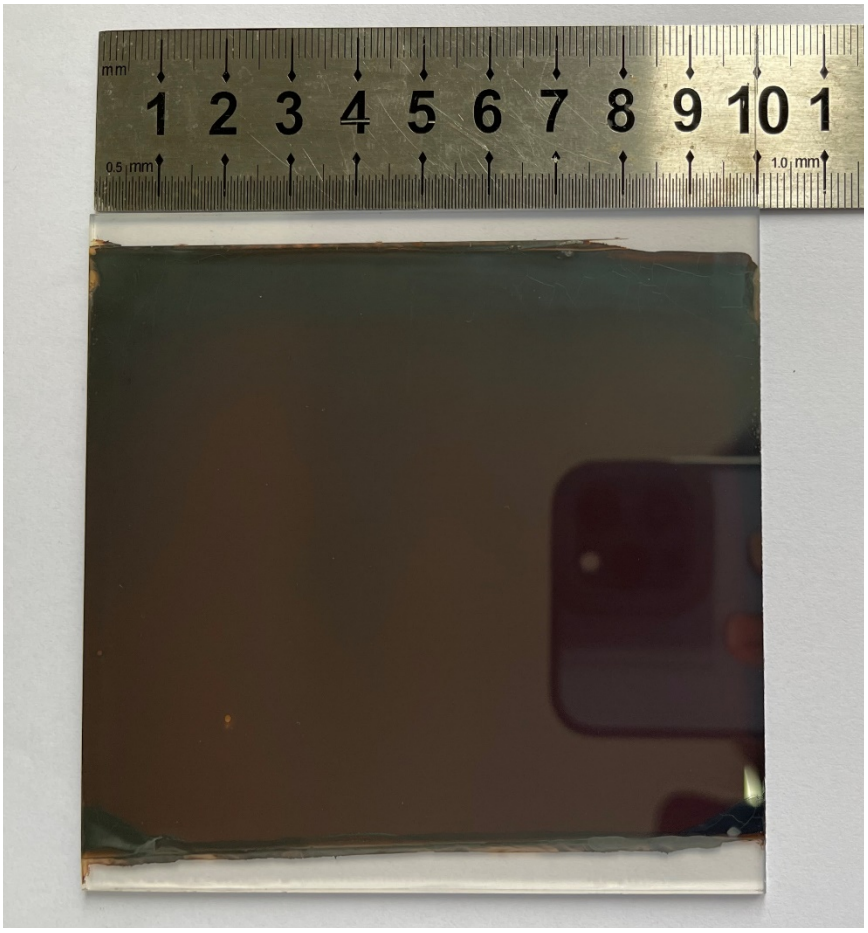

Fig. S13. Photograph of a blade-coated perovskite thin film on a 10 cm × 10 cm substrate.

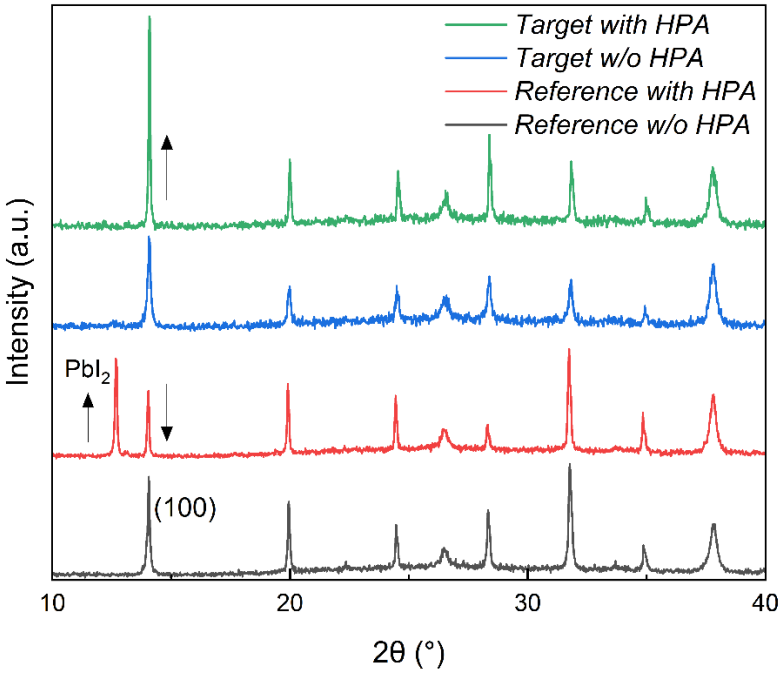

Fig. S14. XRD patterns of $FA_{0.83}Cs_{0.17}Pb(I_{0.9}Br_{0.1})_3$ prepared from PbI_2 route and $PbAc_2$ route, with and without HPA addition (11.25 mol% HPA with respect to Pb).

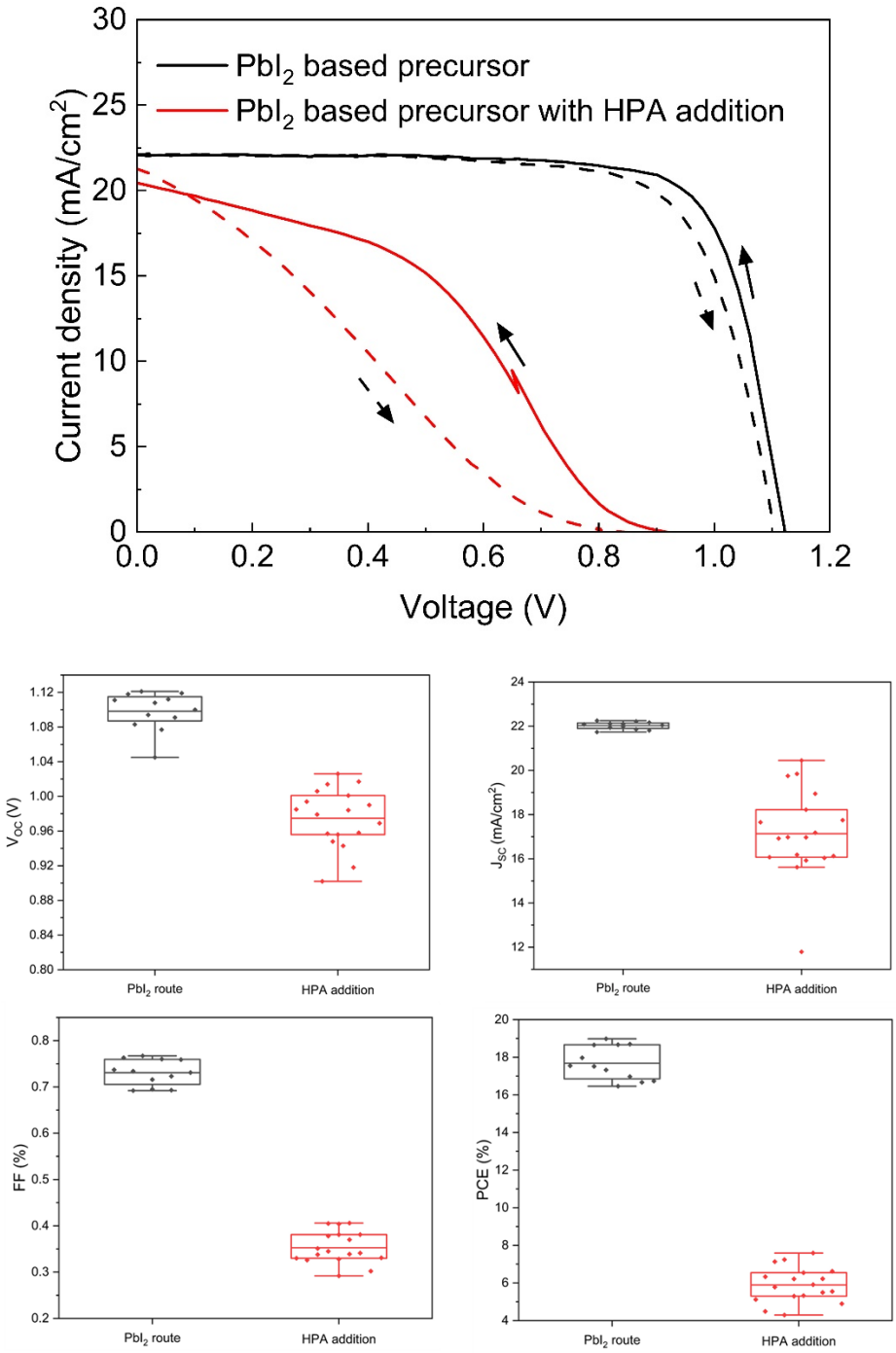

Fig. S15. The photovoltaic performance of PSCs prepared from PbI_2 route with and without HPA addition. (11.25 mol% HPA with respect to Pb). Statistic device parameters are obtained from the reverse J-V scan.

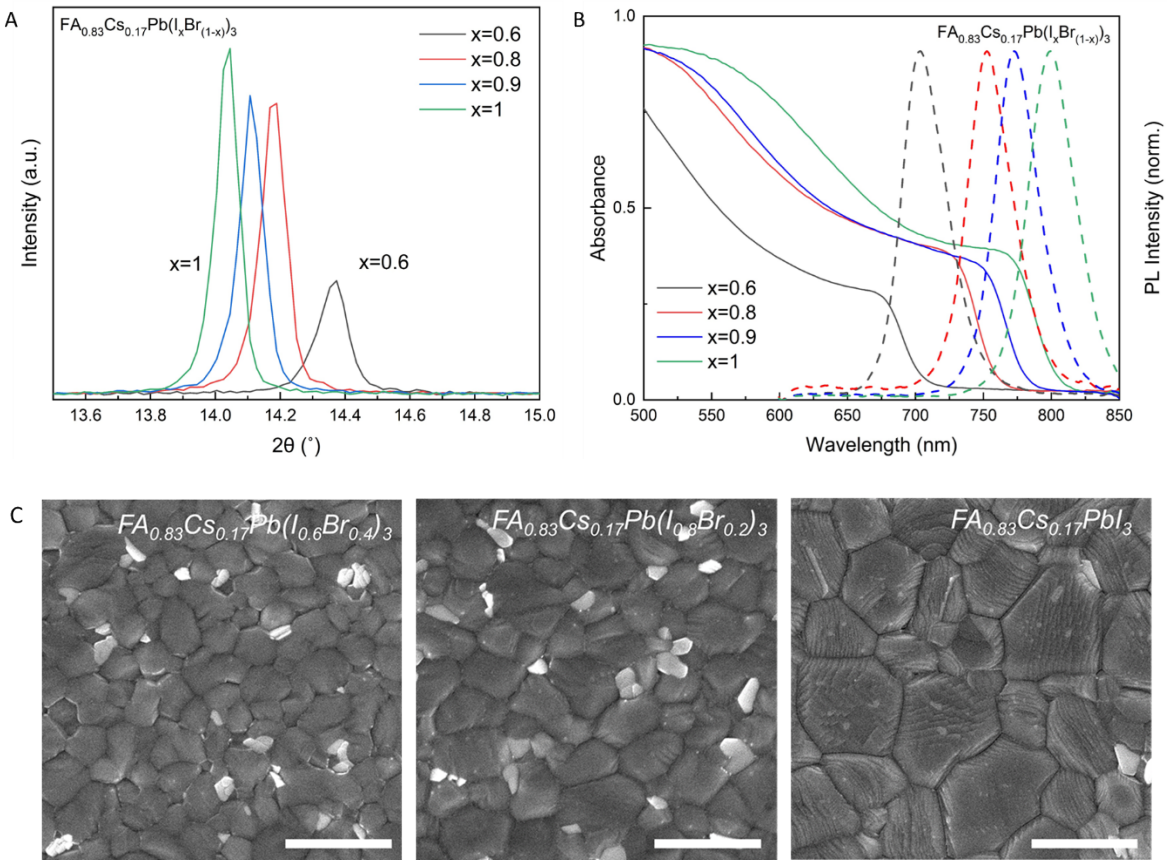

Fig. S16. Characterization of $FA_{0.83}Cs_{0.17}Pb(I_xBr_{(1-x)})_3$ films made from $PbAc_2$ route with different Br composition. (**A**) XRD patterns. (**B**) UV-vis absorption and PL spectra. (**C**) SEM (Scale Bar: 1μm).

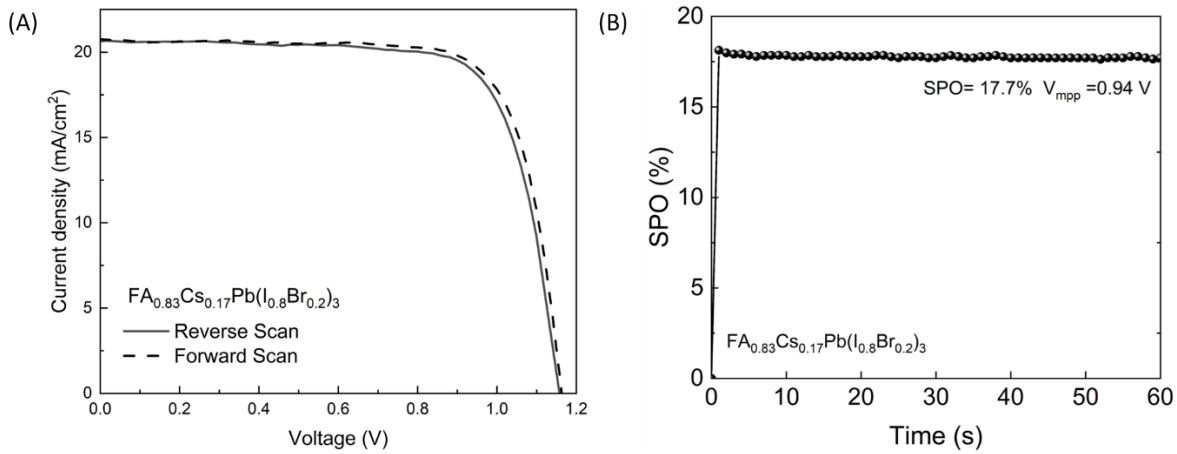

Fig. S17. $FA_{0.83}Cs_{0.17}Pb(I_{0.8}Br_{0.2})_3$ device photovoltaic performance. (A) *J-V* characteristics of champion $FA_{0.83}Cs_{0.17}Pb(I_{0.8}Br_{0.2})_3$ device. (PCE: 17.8% (reverse) 18.1% (forward)) (B) Stabilized power output (SPO) of champion $FA_{0.83}Cs_{0.17}Pb(I_{0.9}Br_{0.1})_3$ device.

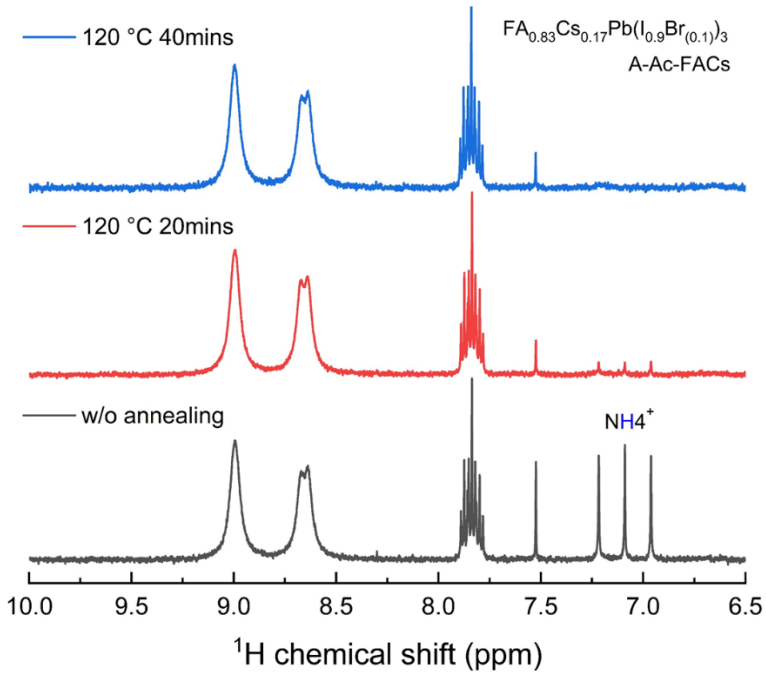

Fig. S18. Solution ^{1}H NMR spectra of $FA_{0.83}Cs_{0.17}Pb(I_{0.9}Br_{0.1})_3$ films made via $PbAc_2$ route after coating (black), annealed at 120 °C for 20 min (red) and 40 min (blue), respectively. The films were dissolved in DMSO-d_6 for the measurement.

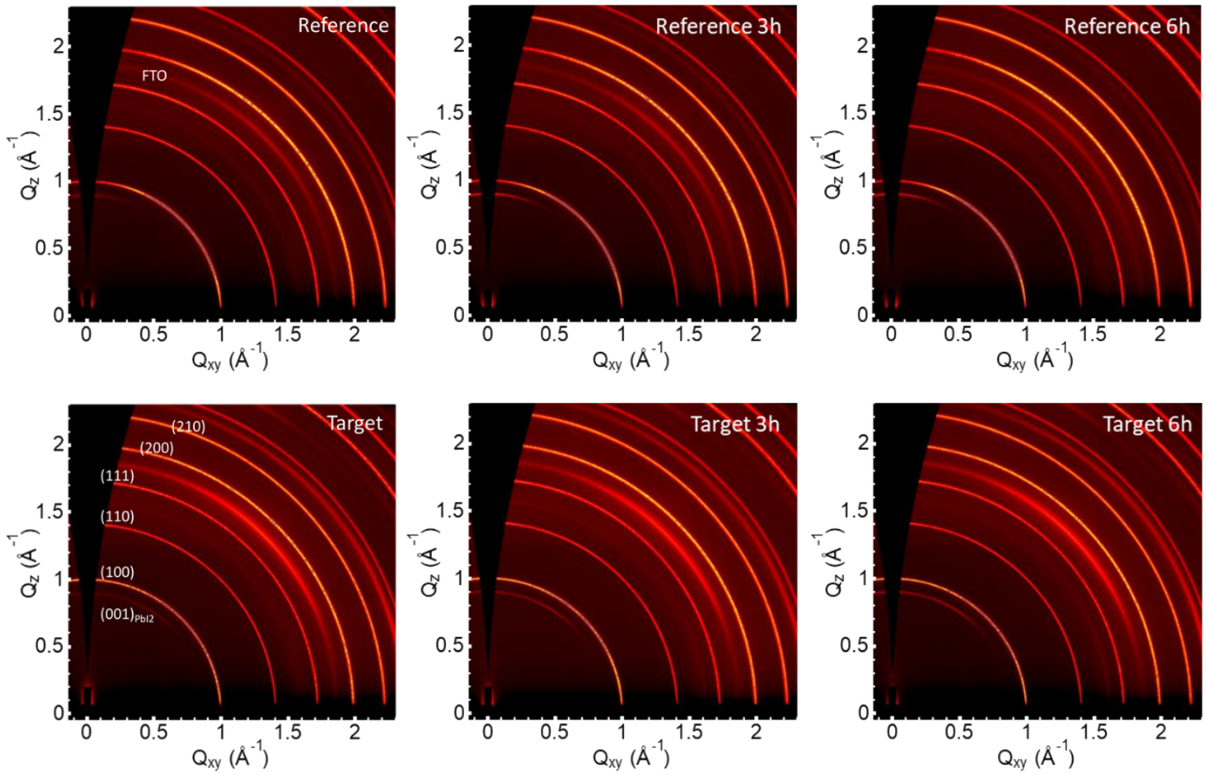

Fig. S19. Two-dimensional grazing-incidence wide-angle X-ray scattering (GIWAXS) patterns of the reference and target $FA_{0.83}Cs_{0.17}Pb(I_{0.9}Br_{0.1})_3$ films. Perovskite thin films were thermally aged at 130°C in N_2 environment.

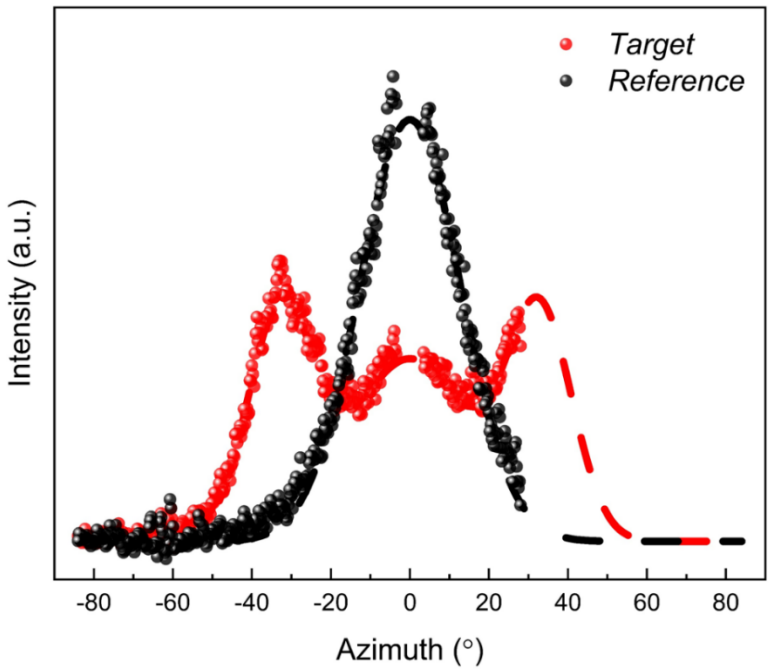

Fig. S20. Pole figure of PbI_2 (001) peak in fresh perovskite films integrated azimuthally along q ~ 0.9 Å^{-1}.

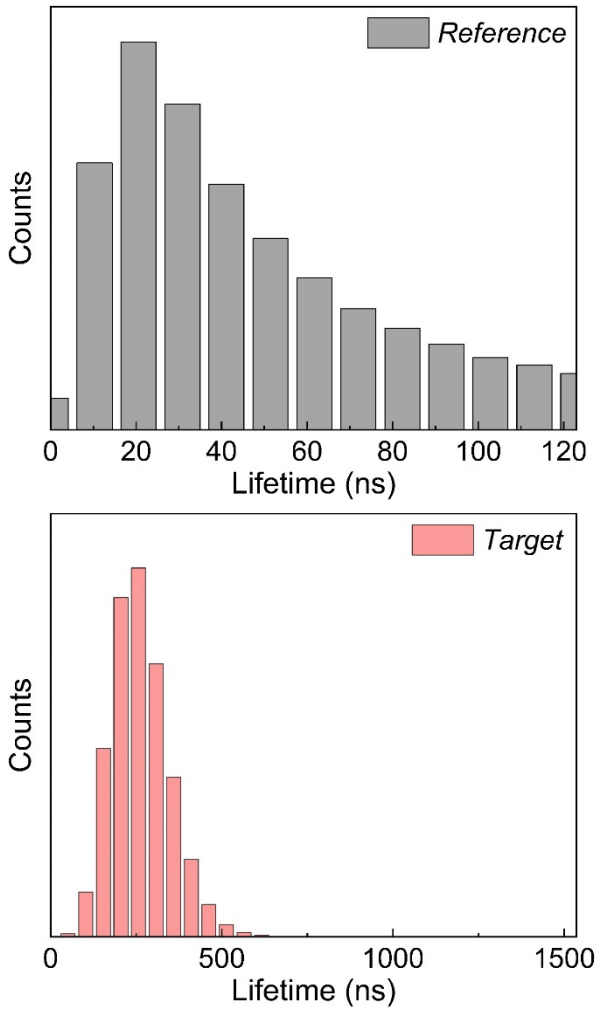

Fig. S21. FLIM: Carrier lifetime histogram.

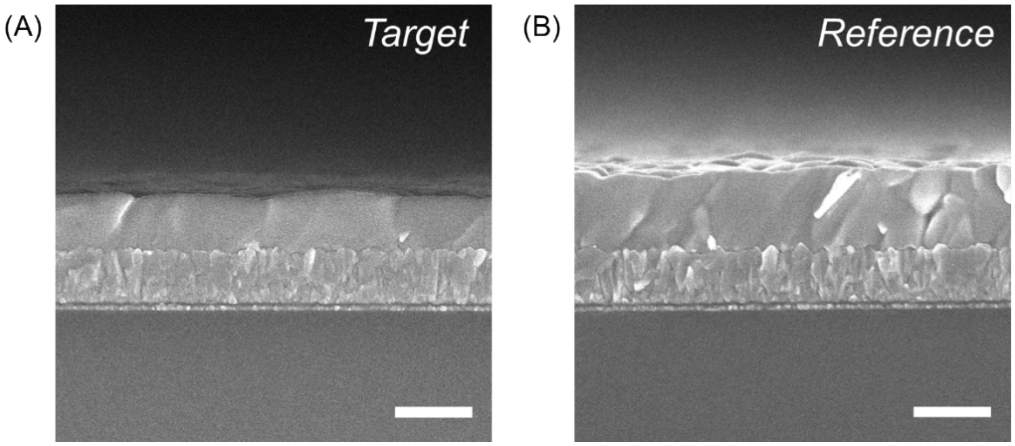

Fig. S22. Cross sectional SEM of perovskite thin films. (Scale Bar: 500nm)

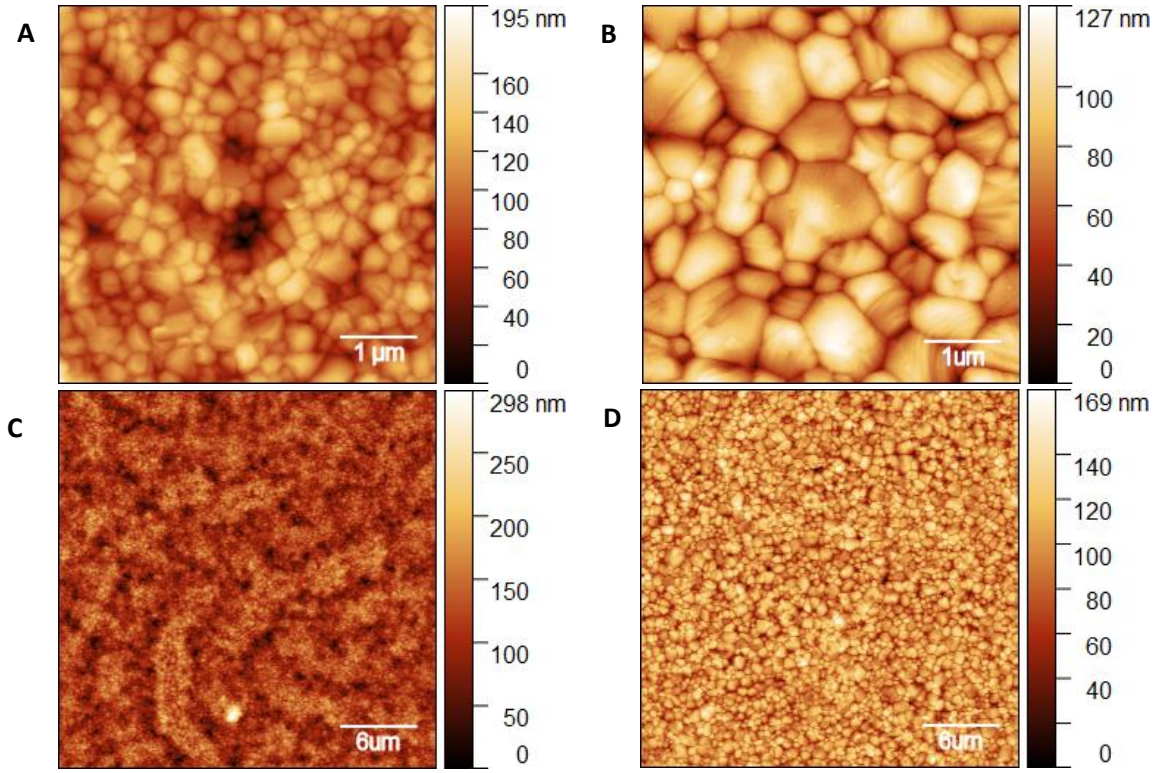

Fig. S23. Atomic force microscopy (AFM) images. (**A** and **B**) $FA_{0.83}Cs_{0.17}Pb(I_{0.9}Br_{0.1})_3$ film made from PbI_2 route (A) and $PbAc_2$ route (B). Scan area: 5 µm × 5 µm. (**C** and **D**) $FA_{0.83}Cs_{0.17}Pb(I_{0.9}Br_{0.1})_3$ film made from PbI_2 route (C) (RMS roughness: 28.42nm) and $PbAc_2$ route (D) (RMS roughness: 19.34nm). Scan area: 30 µm × 30 µm.

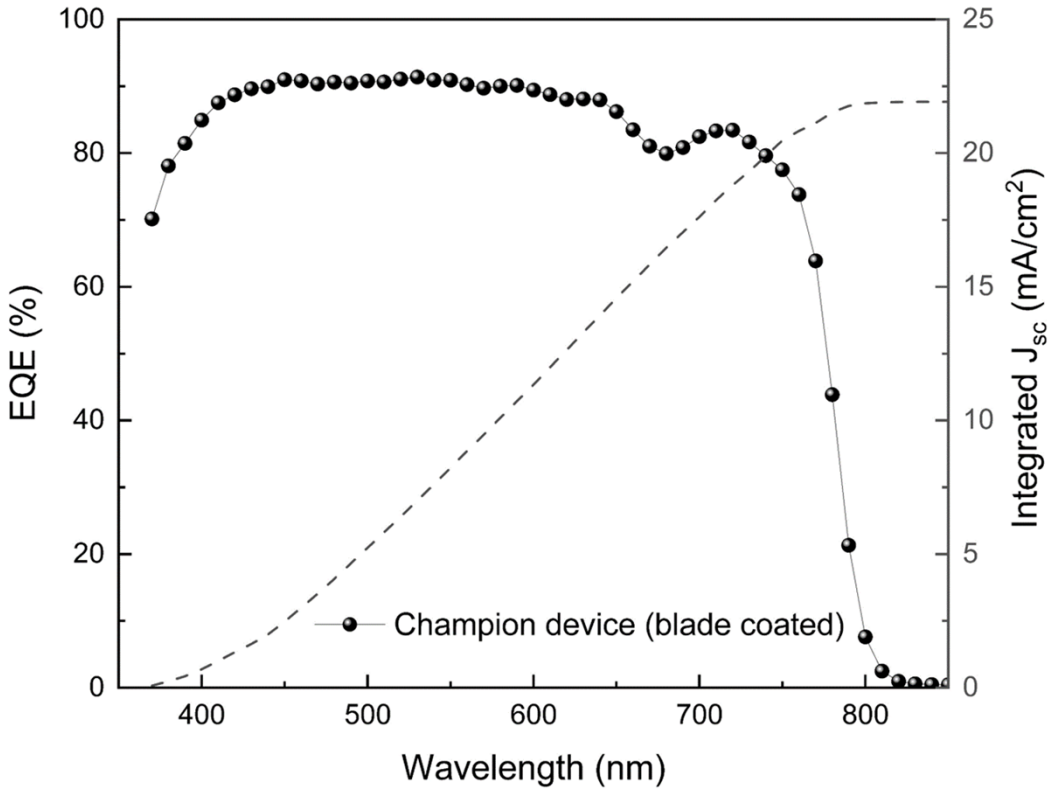

Fig. S24. EQE and the integrated J_{SC} of the champion device.

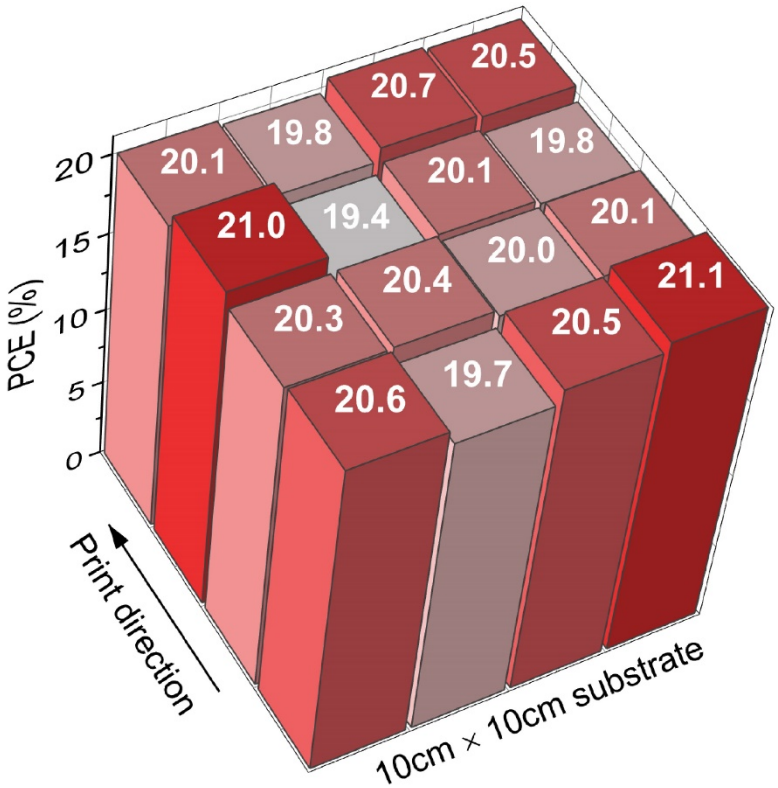

Fig. S25. The distribution of the PCEs of 16 sub-cells on a 10cm*10cm substrate.

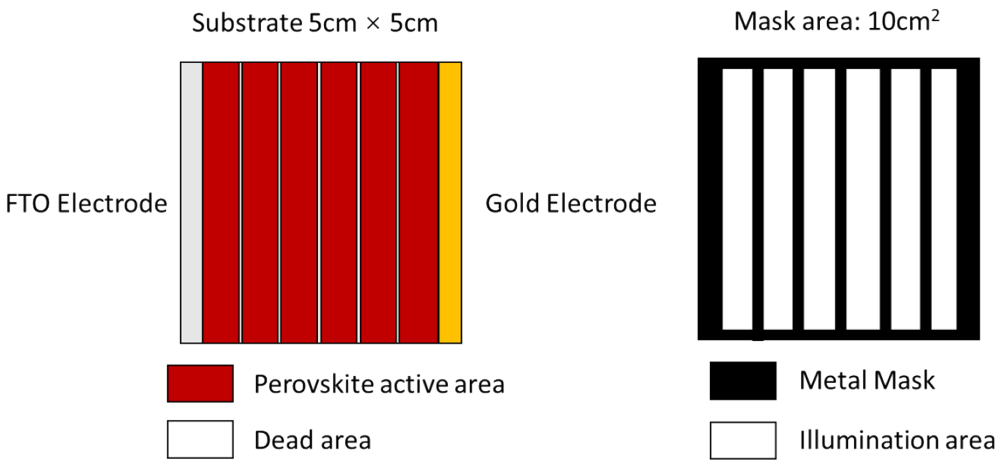

Fig. S26. The sketch of the top view of module and metal mask.

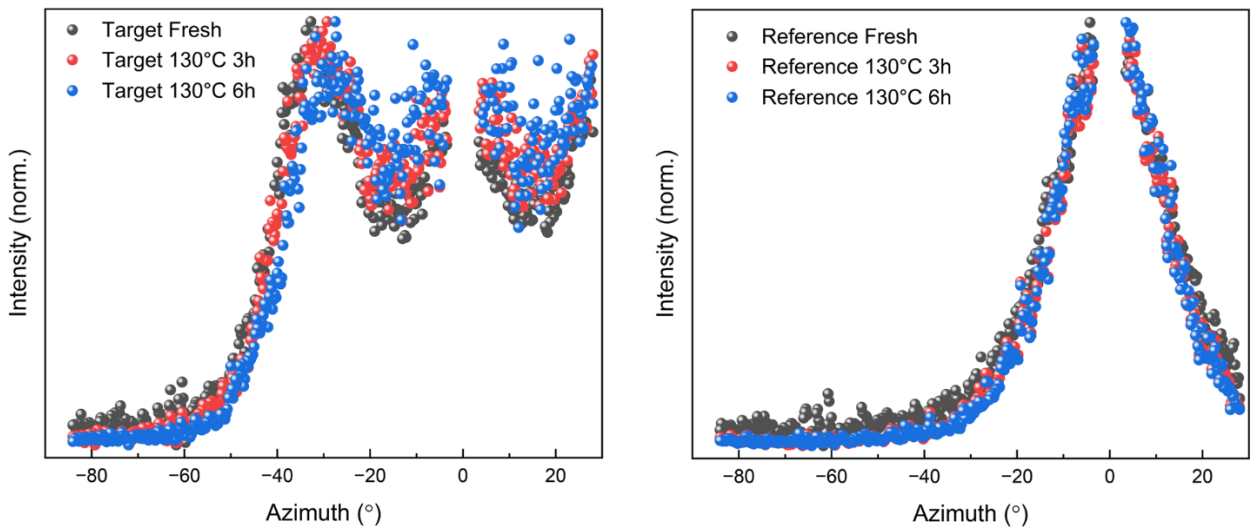

Fig. S27. Pole figure of PbI_2 (001) peak in fresh and thermally aged perovskite films integrated azimuthally along q ~ 0.9 Å^{-1}.

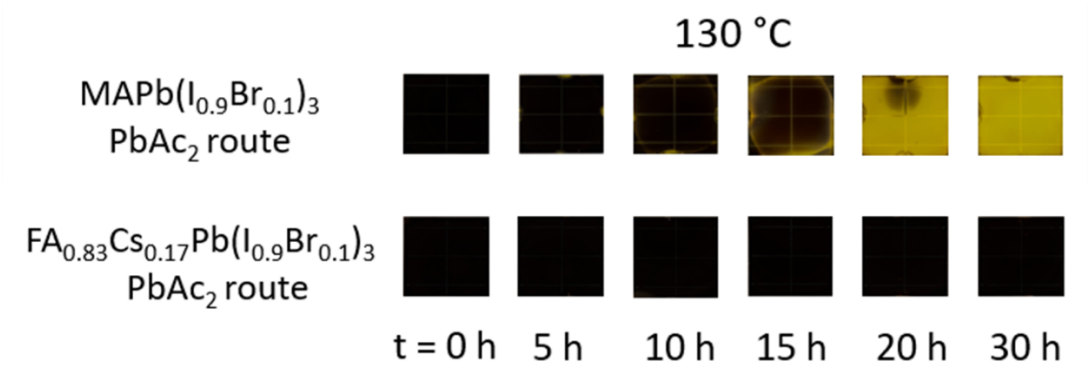

Fig. S28. Photographs of perovskite thin films (thermally aged at 130 °C in nitrogen environment under dark condition).

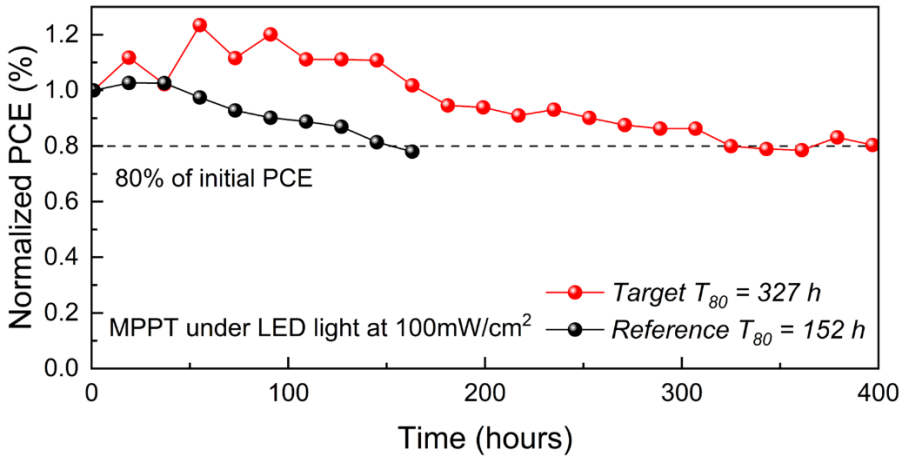

Fig. S29. Long-term device operational stability test. The devices were kept at room temperature without active cooling in a N_2 environment. PTAA was used to replace spiro-OMeTAD in the normal structured (*p-i-n*) device.

Table S1. Summary of the PCE of PSCs made from non-halide lead source-based precursor solution.

Lead Source	Perovskite composition	PCE (%)	Reference
$Pb(SCN)_2$	$MAPb(SCN)_2I$	8.3	(3)
$Pb(SCN)_2$	$MAPbI_3$	7.6	(4)
$Pb(SCN)_2$	$MAPb(SCN)_xI_{3-x}$	15.1	(5)
$Pb(NO_3)_2$	$MAPbI_3$	12.6	(6)
$Pb(NO_3)_2$	$MAPbI_3$	8.4	(4)
$Pb(acac)_2$	$MAPbI_3$	1.5	(7)
$Pb(HCOO)_2$	$MAPbI_3$	20.3	(8)
$Pb(Ac)_2$	$MAPbI_3$	10.8	(7)
$Pb(Ac)_2$	$MAPbI_3$	12.5	(9)
$Pb(Ac)_2$	$MAPbI_3$	15.2	(10)
$Pb(Ac)_2$	$MAPbI_3$	16.2	(11)
$Pb(Ac)_2$	$MAPbI_3$	18.0	(12)
$Pb(Ac)_2$	$MAPbI_{3-x}Br_x$	18.7	(13)
$Pb(Ac)_2$	$MAPbI_{3-x}Br_x$	18.3	(14)
$Pb(Ac)_2$	$MAPbI_3$	11.6	(15)
$Pb(Ac)_2$	$MAPbI_{3-x}Br_x$	16.3	(16)
$Pb(Ac)_2$	$MAPbI_3$	18.5	(17)
$Pb(Ac)_2$	$CsPbI_3$	12.9	(18)
$Pb(Ac)_2$	$FA_{0.83}Cs_{0.17}Pb(I_{0.9}Br_{0.1})_3$	21.0	This work

Table S2. Summary of the processing parameters for P1, P2, P3 laser cutting

	Scanning speed (mm/s)	Power (W)	Repeat frequency (kHz)
P1	500	80	20
P2	1000	30	80
P3	1000	30	80

EXPERIMENTAL PROCEDURES

Materials

Unless otherwise specified, all materials were purchased from either Alfa Aesar or Sigma-Aldrich without any further purification. Formaminidium iodide (FAI), formamidinium bromide (FABr), methylammonium iodide (MAI) were purchased from Greatcell Solar Ltd. Poly(triaryl amine) (PTAA) (Mn<6000 and 15000<Mn<30000) and *iso*-butylammonium bromide (*i*-BABr) were purchased from Xi'an Polymer Light Co., Ltd. Lead acetate ($PbAc_2$) was purchased from TCI. Spiro-OMeTAD and FK209 Co(III) TFSI Salt were purchased from Luminescence Technology Corp. 4-isopropyl-4'-methyldiphenyliodonium Tetrakis(pentafluorophenyl) borate (TPFB) was purchased from TCI.

Preparation of precursor solutions

$PbAc_2$ based precursor solutions: The precursor solutions were prepared in N_2 glovebox by mixing stoichiometric amount of FABr, FAI, CsI and $PbAc_2$ in anhydrous *N,N*-dimethylformamide (DMF) with further addition of FAI, MAI and NH_4I at a molar ratio of 2:1 (with respect to Pb^{2+}) as volatile organic salts for FA-Ac-FACs, MA-Ac-FACs and A-Ac-FACs, respectively. The precursor solution was stirred for 5 min, then three equimolar amounts (relative to Pb^{2+}) of deionized water were added to help dissolve $PbAc_2$ and CsI. The precursor solution was further stirred for 10 min until fully dissolved. Finally, hypophosphorous acid (HPA) solution was added, and the molar ratio of HPA/Pb^{2+} was 11.25%. (19)

PbI_2 based precursor solutions: The 1.45 M precursor solution was prepared in a glovebox by mixing stoichiometric amounts of FAI, CsI, PbI_2 and $PbBr_2$ in a solvent mixture (4:1) of DMF and dimethyl sulfoxide (DMSO). The precursor solution was stirred for 1hour before use.

Device fabrication

FTO glass was cleaned and sonicated with detergent, deionized water, acetone and isopropanol for 15 min each. Then, it was treated by UV-plasma for 15 min before use. The ETL SnO_2 was deposited onto FTO glass by a chemical bath deposition method (CBD). 12 mM of $SnCl_2 \cdot 2H_2O$ with 5 g urea was dissolved in 100 μL of thioglycolic acid, 5 mL of HCl (37%) and 400 mL deionized water to make the precursor solution. The as-cleaned FTO substrate was dipped into the diluted solution (2 mM) for 2.5 hour at 90 °C. Then it was sonicated in deionized water for 5 min followed by the annealing at 180 °C for 1 hour. Then the substrate was treated by UV-plasma for 15 min for the deposition of perovskite. For PbI_2 route, 1.45 M perovskite precursor solution was spin-coated and then annealed at 100 °C for 60mins, according to previous report. (20) For $PbAc_2$ route, 1.1M of A-Ac-FACs solution was spin-coated at 3000rpm of 30s with a ramping speed of 1000rpm/s. For the blade coating, 0.8

M of A-Ac-FACs solution was blade coated at 1.67 mm/s with N_2 knife blowing at room temperature in an ambient air environment. The coating gap is 150 μm, and the gas pressure was controlled at ~0.04 MPa. The as-coated film was then annealed at 120 °C for 40 min. After annealing, for the fabrication of PSCs, large area-substrate (10 cm × 10 cm) coated with perovskite was divided into 16 pieces with each piece having 2.5 × 2.5 cm^2 size. Then 2.5 mg/mL i-BABr in IPA was dynamically spun on top of the perovskite at 5000 rpm for 30 s followed by the annealing at 100 °C for 5 min. For HTL, spiro-OMeTAD (73 mg, 30 μL 4-tert-butylpridine, 18 μL LiTFSI (520 mg/mL in acetonitrile) and 29 μL FK209 (300 mg/mL in acetonitrile) in 1 mL chlorobenzene) was spin-coated at 3000 rpm for 30 s. For the operational stability test, 10mg/mL of PTAA in CB with (10wt% of TPFB) was used to replace spiro-OMeTAD following a previous literature. (21) Finally, an 80 nm gold layer was deposited by thermal evaporation to complete the device. For the thermal stability test, the inverted device architecture was used. PTAA (2 mg/mL in CB) was spin-coated at 2000 rpm for 20 s, and annealed at 150 °C for 10 min as the HTL. Then an Al_2O_3 nanoparticles layer (1:150 v/v ratio Al_2O_3 NPs/IPA) was dynamically spun on PTAA at 4000 rpm for 30 s. A subsequent anneal at 100 °C for 5 min was performed. The deposition of perovskite used the same procedure described before. $PC_{61}BM$ (20 mg/mL in CB) was dynamically spun onto the perovskite layer at a speed of 2000 rpm for 20 s. The samples were then annealed at 100 °C for 5 min. An interlayer of BCP (0.5 mg/mL in IPA) was spin-coated at 5000rpm for 30 s. Finally, an 80 nm gold layer was thermally evaporated.

Module Fabrication

The module was designed to have 6 subcells connected in series with P1, P2 and P3 inter-connections. The FTO glass was first etched by nanosecond laser to from P1 lines. After the deposition of perovskite and spiro-OMeTAD, the P2 lines were formed by laser cutting. Finally, after the Au evaporation, the module was re-etched to form P3 lines. The gap between P1, P2 and P3 are about 200μm. The detailed processing parameter is shown in Table S3.

Material characterization

^{1}H-NMR, ^{1}H-^{1}H COSY, ^{13}C NMR spectra were recorded on a Bruker AVIII 400MHz spectrometer. For perovskite thin film samples, 4 perovskite films were dissolved in DMSO-d_6 for the measurement. Small amount of HI (1μL of 57% w/w HI in 750 μL of DMSO-d_6) was added to get a better quality ^{1}H-NMR spectra. (22)

The external quantum efficiency (EQE) of the PSCs were measured by Fourier transform photocurrent spectroscopy based on a Bruker Vertex 80v Fourier transform spectrometer. A tungsten-halogen lamp was used as the light source and the intensity was calibrated against

a reference silicon photodiode. The wavelength interval we used for the measurement is 10nm.

The GIWAXS experiments were performed at the SAXS/WAXS beamline at the Australian Synchrotron. (23) The beam energy was fixed at 15 keV. The scattering patterns were collected using an in-vacuum Dectris Pilatus 2M detector with a total exposure time of 3 s. The entire beam path from source to sample to detector was placed under vacuum to minimise diffuse air scattering hence improving the signal-to-noise ratio of the scattering patterns. An incident angle of 0.4° which is higher than the critical angle was used to probe the entire depth of the perovskite film. The sample-to-detector distance was calibrated to be ~ 66 cm using a silver behenate standard. Data reduction and analysis was performed using an altered version of NIKA analysis package implemented in Igor. (24)

Uv-vis spectra were collected with a Perkin Elmer Lambda 1050 spectrometer.

The PL emission spectra and time-resolved confocal PL mapping were measured with a Picoquant Microtime 200 instrument with 485nm laser excitation.

TRPL spectra were recorded using a luminescence spectrometer (Edinburgh instruments, FLSP920) with a pulsed diode laser as the excitation source (466 nm). PL was collected using a grating monochromator, and the excitation and PL detection was from the perovskite side. Spectra are corrected for the wavelength-dependence for the detector.

SEM images were taken using a FEI Nova NanoSEM 450 FEG scanning electron microscope with a beam accelerate voltage at 5kV.

AFM images were collected with a Dimension iCon AFM in tapping mode in the air. For the thermal stability test, the encapsulated devices were placed on a 65°C hot plate in the air.

The X-ray diffraction (XRD) data was collected by using a Bruker D8 Advance diffractometer in Brag-Brentano geometry. A Cu-$k\alpha$ (λ = 0.15406 nm) radiation was used with a generator voltage at 40kV and current at 40mA. Diffraction data was collected by a Lyxeye XE position sensitive detector in 1D mode. As the sample film was prepared with a thickness that the X-ray beam is able to penetrate through, this is evident with the substrate diffraction peaks can always been visible. A dynamic divergence slit size was used to maintain a constant beam illumination size at 9 mm. In-situ XRD data was collected with sample thermally aged under 130 °C in dried N_2 environment in an MTC wide range variable temperature chamber. The XRD data was analysed using a Rietveld refinement software TOPAS Academic version 7. Pawley refinement was used to refine the perovskites phase with a cubic crystalline structure with a space group of *Pm-3m*. The microstrain and crystallite size were extracted from the

refinement results with calculated errors. The environmental contribution for in-situ XRD pattern was measured and has been modelled in the refinement.

Device characterization

The photovoltaic performance was measured under 1-sun illumination (100 mW/cm^{-2}) using an Oriel solar simulator equipped with a xenon lamp and an AM 1.5G filter. The light intensity was calibrated by a standard silicon reference solar cell (Oriel, VLSI standards). The *J-V* characteristics were performed with forward and reverse scan between -0.1 to 1.2V with a voltage step of 10mV and settling time of 100ms (100mV/s) by a Keithley 2400 source meter. All devices were tested using a black metal mask with an aperture area of 0.16cm^2 and 10cm^2 for small area devices and solar modules, respectively.

Supplementary Reference

1. Wang, Xiao et al., 2020. Perovskite Solution Aging: What Happened and How to Inhibit? Chem, 6(6), pp.1369–1378.

2. Grundmann, Christoph & Kreutzberger, Alfred, 1955. Triazines. XIII. The Ring Cleavage of s-Triazine by Primary Amines. A New Method for the Synthesis of Heterocycles1,2. *Journal of the American Chemical Society*, 77(24), pp.6559–6562.

3. Jiang Q, Rebollar D, Gong J, Piacentino EL, Zheng C, Xu T. Pseudohalide-Induced Moisture Tolerance in Perovskite $CH_3NH_3Pb(SCN)_2I$ Thin Films. Angewandte Chemie International Edition. 2015;54(26):7617-20.

4. Balaji G, Joshi PH, Abbas HA, Zhang L, Kottokkaran R, Samiee M, et al. $CH_3NH_3PbI_3$ from non-iodide lead salts for perovskite solar cells via the formation of PbI2. Physical Chemistry Chemical Physics. 2015;17(16):10369-72.

5. Tai Q, You P, Sang H, Liu Z, Hu C, Chan HLW, et al. Efficient and stable perovskite solar cells prepared in ambient air irrespective of the humidity. Nature Communications. 2016;7(1):11105.

6. Hsieh T-Y, Wei T-C, Wu K-L, Ikegami M, Miyasaka T. Efficient perovskite solar cells fabricated using an aqueous lead nitrate precursor. Chemical Communications. 2015;51(68):13294-7.

7. Aldibaja FK, Badia L, Mas-Marzá E, Sánchez RS, Barea EM, Mora-Sero I. Effect of different lead precursors on perovskite solar cell performance and stability. Journal of Materials Chemistry A. 2015;3(17):9194-200.

8. Gu J, Li F, Wang Z, Xie Y, Yan L, Zeng P, et al. Morphology Tuning and Its Role in Optimization of Perovskite Films Fabricated from A Novel Nonhalide Lead Source. Advanced Science. 2020;7(23):2002296.

9. Forgács D, Sessolo M, Bolink HJ. Lead acetate precursor based p-i-n perovskite solar cells with enhanced reproducibility and low hysteresis. Journal of Materials Chemistry A. 2015;3(27):14121-5.

10. Zhang W, Saliba M, Moore DT, Pathak SK, Hörantner MT, Stergiopoulos T, et al. Ultrasmooth organic–inorganic perovskite thin-film formation and crystallization for efficient planar heterojunction solar cells. Nature Communications. 2015;6(1):6142.

11. Zhang W, Pathak S, Sakai N, Stergiopoulos T, Nayak PK, Noel NK, et al. Enhanced optoelectronic quality of perovskite thin films with hypophosphorous acid for planar heterojunction solar cells. Nature Communications. 2015;6(1):10030.

12. Singh T, Miyasaka T. High performance perovskite solar cell via multi-cycle low temperature processing of lead acetate precursor solutions. Chemical Communications. 2016;52(26):4784-7.

13. Chen K, Hu Q, Liu T, Zhao L, Luo D, Wu J, et al. Charge-Carrier Balance for Highly Efficient Inverted Planar Heterojunction Perovskite Solar Cells. Advanced Materials. 2016;28(48):10718-24.

14. Zhao L, Luo D, Wu J, Hu Q, Zhang W, Chen K, et al. High-Performance Inverted Planar Heterojunction Perovskite Solar Cells Based on Lead Acetate Precursor with Efficiency Exceeding 18%. Advanced Functional Materials. 2016;26(20):3508-14.

15. Hu Q, Zhao L, Wu J, Gao K, Luo D, Jiang Y, et al. In situ dynamic observations of perovskite crystallisation and microstructure evolution intermediated from $[PbI_6]^{4-}$ cage nanoparticles. Nature Communications. 2017;8(1):15688.

16. Li C, Guo Q, Wang Z, Bai Y, Liu L, Wang F, et al. Efficient Planar Structured Perovskite Solar Cells with Enhanced Open-Circuit Voltage and Suppressed Charge Recombination Based on a Slow Grown Perovskite Layer from Lead Acetate Precursor. ACS Applied Materials & Interfaces. 2017;9(48):41937-44.

17. Giesbrecht N, Schlipf J, Grill I, Rieder P, Dyakonov V, Bein T, et al. Single-crystal-like optoelectronic-properties of MAPbI3 perovskite polycrystalline thin films. Journal of Materials Chemistry A. 2018;6(11):4822-8.

18. Xie H, Xu J, Gao C, Zhang J, Gao C, Liu X. Lead acetate precursors for preparing $CsPbI_3$ light harvester layers of inorganic perovskite solar cells. Solar Energy. 2021;222:212-8.

19. Zhang, Wei et al., 2015. Enhanced optoelectronic quality of perovskite thin films with hypophosphorous acid for planar heterojunction solar cells. Nature communications, 6(1), p.10030.

20. Lin, Yen-Hung et al., 2020. A piperidinium salt stabilizes efficient metal-halide perovskite solar cells. Science (American Association for the Advancement of Science), 369(6499), pp.96–102.

21. Wang, Rui et al., 2019. Constructive molecular configurations for surface-defect passivation of perovskite photovoltaics. Science (American Association for the Advancement of Science), 366(6472), pp.1509–1513.

22. Van Gompel WTM, Herckens R, Reekmans G, Ruttens B, D'Haen J, Adriaensens P, et al. Degradation of the Formamidinium Cation and the Quantification of the Formamidinium–Methylammonium Ratio in Lead Iodide Hybrid Perovskites by Nuclear Magnetic Resonance Spectroscopy. The Journal of Physical Chemistry C. 2018;122(8):4117-24.

23. Kirby, Nigel M et al., 2013. A low-background-intensity focusing small-angle X-ray scattering undulator beamline. Journal of applied crystallography, 46(6), pp.1670–1680.

24. Ilavsky, Jan, 2012. Nika: software for two-dimensional data reduction. Journal of applied crystallography, 45(2), pp.324–328.